

Contrasting Characteristics of Convection over the Northern and Southern South China Sea during SCSMEX

PAUL E. CIESIELSKI AND RICHARD H. JOHNSON

Department of Atmospheric Science, Colorado State University, Fort Collins, Colorado

(Manuscript received 5 April 2005, in final form 19 August 2005)

ABSTRACT

Observations from two enhanced sounding arrays during the May–June 1998 South China Sea Monsoon Experiment (SCSMEX) are used to determine and contrast the properties of convection over the northern and southern South China Sea (SCS). A regression analysis between SST data and monthly rainfall indicates that the ENSO signal exerted a strong influence on the rainfall distribution over the SCS during SCSMEX. This resulted in wetter-than-normal conditions along the south China coast and northern SCS, and generally drier-than-average conditions elsewhere, particularly over the Philippine Islands.

The monsoon onset as determined by a shift in the low-level winds from easterly to southwesterly over the SCS occurred around mid-May. Over the southern enhanced sounding array (SESA), the onset was characterized by a rainy period associated with the passage of a convectively coupled Kelvin wave. This was followed by a weeklong break and then several episodic rain events with increasingly higher rain rates. Rainfall over the northern enhanced sounding array (NESA), which was largely out of phase with SESA rainfall events, occurred primarily during two 10-day periods separated by a weeklong break. Convective characteristics over the SESA, deduced primarily from heat and moisture budget profiles, indicate a high stratiform rain fraction consisting of alternating periods with decaying mesoscale systems that organized near the western Borneo coastline and shallower convective clouds. In contrast, NESA-averaged profiles were indicative of deep convection with a relatively small stratiform rain fraction, which was confirmed with radar analyses during the onset convective period.

The diurnal cycle of convection is a dominant feature throughout much of the SCS. Over both budget regions, early morning (0500–0800 LT) convective systems were frequently initiated near the coasts, then gradually dissipated during the course of the day as the midlevel steering currents moved the systems away from the coastline. These decaying convective systems resulted in an early afternoon (1400 LT) rainfall peak over both sonde arrays.

1. Introduction

The Asian summer monsoon (ASM) is composed of the south Asian (or Indian) monsoon system, the east Asian (or mei-yu–baiu) monsoon system, and the Southeast Asian monsoon (SEAM) system, which covers the South China Sea (SCS) and surrounding landmasses. The ASM is established first over the SCS, typically around mid-May, eventually spreading north over mainland China and westward over India (Tao and Chen 1987). The SEAM is generally regarded as the first stage of the east Asian monsoon and an eastward

extension of the Indian monsoon (Chen and Chen 1995; Chang and Chen 1995).

Several field programs, such as the summer and winter monsoon experiment (MONEX) held in 1978–79, have greatly added to our understanding of the ASM and its convective systems (e.g., Fein and Kuettner 1980; Houze et al. 1981; Johnson and Young 1983; Luo and Yanai 1983, 1984). Despite the significant progress made through these experiments and numerous monsoon studies, the lack of attention prior to the mid-1990s to the late spring season and the monsoon's onset over the SCS has resulted in an incomplete picture of the ASM with no clear consensus on the mechanisms for the onset of the SEAM (Wu and Zhang 1998; Li and Wu 2000). With the ultimate goal to obtain a comprehensive description of the ASM to improve its prediction, the South China Sea Monsoon Experiment (SCS-

Corresponding author address: Paul E. Ciesielski, Department of Atmospheric Science, Colorado State University, Fort Collins, CO 80523.

E-mail: paulc@atmos.colostate.edu

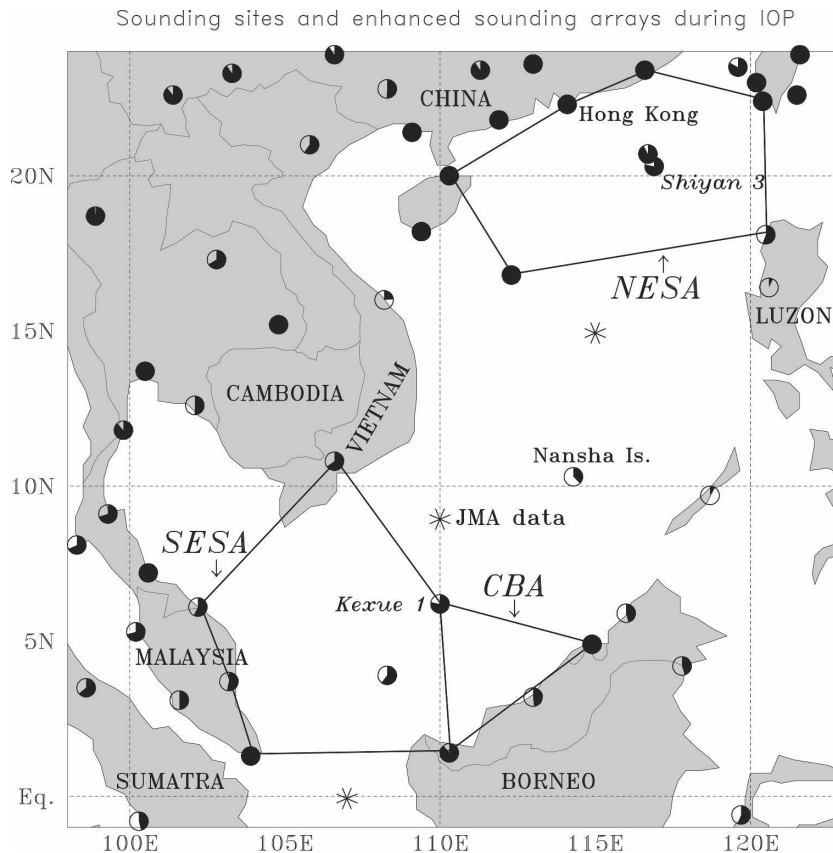


FIG. 1. Sounding sites and enhanced sounding networks during the SCSMEX 47-day IOP. The number of sonde observations during this period is indicated by the filling of circles, where a completely filled circle denotes 188 sonde observations (i.e., 4 sondes day^{-1} for 47 days). The * symbol indicates where JMA/GAME reanalysis values are used to supplement the sounding data.

MEX; Lau et al. 2000) was designed to investigate processes associated with the onset and development of the SEAM in May and June 1998.

While numerous budget studies have examined rainfall and latent heating distributions in the Indian monsoon (e.g., Luo and Yanai 1983, 1984; Yanai and Tomita 1998; Yanai et al. 1992) and east Asian monsoon systems (e.g., Kato 1985; Ding and Wang 1988; Ding and Hu 1988; Johnson et al. 1993), little is known about the contribution to the ASM heat source that extends over the SCS. During the 47-day intensive observing period (IOP) of SCSMEX (5 May–20 June), enhanced budget networks denoted by the polygons in Fig. 1 were established over the SCS to determine and contrast the properties of convection in two distinct oceanic regions of the ASM. These sounding networks include the northern enhanced sounding array (NESA), the southern enhanced sounding array (SESA), and the coastal Borneo array (CBA). Previous analyses from SCSMEX (Johnson and Ciesielski 2002; Wang 2004; Tao et al.

2003; Johnson et al. 2005) have focused on results over the NESA due to better data coverage from both atmospheric soundings and overpasses from the Tropical Rainfall Measuring Mission (TRMM) satellite and the presence of a dual-Doppler radar array in this region. Despite the more limited data over the southern SCS, the opportunity exists to investigate the properties of convection over this region as well. This paper reports on these recent findings and compares various analyses from these two oceanic regions in SCSMEX.

Past studies, using primarily reanalysis products and satellite-derived rainfall estimates, have examined the temporal evolution of the monsoon and the spatial distribution of rainfall over the SCS and surrounding land areas (e.g., Lau and Yang 1997; Wu and Zhang 1998; Fukutomi and Yasunari 1999; Lau and Wu 2001). A common finding in these studies is that convective variability over the SCS is related to large-scale convective and circulation features that encompass the entire Asian–Pacific region. Nitta (1987) showed that Rossby

waves generated by convection over the SCS/west Pacific region result in wavelike variations in the height field and convection that extend northward into the East China Sea and Japan. On the other hand, Lau and Chan (1986) found that convective activity over the Indian monsoon region oscillates inversely with that over the SCS/west Pacific region on a 30–60-day time scale. In a series of papers (Chen and Chen 1995; Chen and Weng 1999; Chen et al. 2000) it was shown that convection over the SCS and east Asia is regulated by northward-propagating 30–60-day monsoon trough/ridge patterns and by an eastward-propagating 12–24-day signal. During SCSMEX these intraseasonal modes appeared to play a role in the timing of the monsoon onset and periods of active and suppressed convection (Loechl 2000; Chan et al. 2002). In addition, Lau et al. (1988) and Chen and Murakami (1988) found that the northward progression of the monsoon into east Asia is not steady in time but rather is characterized by abrupt stepwise shifts that are modulated by intraseasonal modes. Recently, an analysis of global rainfall and sea surface temperature (SST) data by Lau and Wu (2001) showed that on the average ENSO-related basin-scale SSTs together with regional processes account for nearly half of the variance of deseasonalized monthly rainfall anomalies over the ASM region. Since SCSMEX occurred during a period of strong ENSO variability, its impact on the distribution of rainfall over the SCS will be examined in this paper.

The focus of this study is on the characteristics of convection over the northern and southern portions of the SCS as deduced from analyses derived primarily from the SCSMEX sounding dataset. The remainder of this paper is organized as follows. In section 2, the datasets and analysis procedures used in this present study are described. A discussion of the large-scale circulation and rainfall patterns accompanying the 1998 monsoon and its onset over the SCS is given in section 3. In section 4 the focus is on the temporal variability of various surface and upper-level fields over the SCS. This discussion is expanded in section 5 where SCSA-averaged rainfall time series and budget profiles are compared to similar products from the NESAs. Since SCSMEX was the first TRMM field campaign, and one of the primary goals of TRMM is to determine rainfall distributions (Kummerow et al. 2000) and four-dimensional patterns of latent heating over the Tropics (Olson et al. 1999; Shige et al. 2004), particular attention is given to budget-derived heating profiles and comparisons between rainfall estimates from the moisture budget and TRMM. The prominent land features that encompassed the SCS give rise to a notable diurnal

cycle over this region. In section 6 the diurnal cycle of convection over the SCS is examined with an emphasis on its characteristics over the southern SCS. A summary and some concluding remarks are offered in section 7.

2. Data and analysis procedures

a. Sounding networks

Three budget networks were selected (Fig. 1) to optimize the use of the sounding data and to focus on the effects of oceanic convection.¹ During the 47-day SCSMEX IOP, the majority of the sounding sites within these networks launched four sondes per day. The filling of the circles in Fig. 1 indicates the number of sonde observations at the various sites during the IOP. Two research vessels (R/Vs) provided hourly surface fluxes in addition to four high-vertical-resolution sondes per day. The NESAs were centered around the R/V *Shiyan* #3, which was nominally located at 20.4°N, 117°E. A second research vessel, positioned at 6.2°N, 110°E, was originally intended to be near the center of a southern sounding network. Unfortunately, problems with the sonde equipment at Nansha Island (location shown in Fig. 1) resulted in little useful data at this site, such that the SCSA was reconfigured to have the R/V *Kexue* #1 on its perimeter. These ships were on location from 5 May through 20 June with the exception of a 9-day port call near the end of May. While the NESAs were composed of a variety of sonde types, the perimeter sites of the SCSA all used Vaisala RS80-type sondes. A third sounding network, the CBA, was constructed to examine the diurnal cycle of oceanic convection off the northwest coast of Borneo.

b. Objective analysis and computation of diagnostic quantities

Gridded fields of the horizontal wind components (u and v), temperature (T), specific humidity (q), and geopotential height (z) were analyzed at 6-h, 1° horizontal, 25-hPa vertical resolution over the SCSMEX domain (10°S–40°N, 80°–130°E). To assist the objective analysis in data-sparse oceanic regions, reanalysis values from the Japan Meteorological Agency (JMA) Global Energy and Water Cycle Experiment (GEWEX) Asian Monsoon Experiment (GAME) V1.1 reanalysis (Yamazaki et al. 2000) available at 6-h resolution were used at a few selected locations (shown in Fig. 1) that are outside the budget polygons. Additional details of

¹ Averages computed over the budget networks in this study excluded any land points that were within these polygons.

the objective analysis scheme used here, as well as the procedures for quality controlling the sonde data, mass balancing the divergence field (δ), and computing the vertical p velocity (ω) are described in Johnson and Ciesielski (2002, hereafter referred to as JC02).

In this study the heat and moisture budgets were computed using the gridded dataset following Yanai et al. (1973). Here the apparent heat source (Q_1) is defined as $c_p[\partial\bar{T}/\partial t + \bar{\mathbf{v}} \cdot \nabla\bar{T} + (p/p_0)^\kappa \bar{\omega}\partial\theta/\partial p]$, and the apparent moisture sink (Q_2) is defined as $-L(\partial\bar{q}/\partial t + \bar{\mathbf{v}} \cdot \nabla\bar{q} + \bar{\omega}\partial\bar{q}/\partial p)$, where $\kappa = R/c_p$, R is the gas constant, c_p the specific heat at constant pressure for moist air, L the latent heat of vaporization, and the overbar denotes a horizontal average.

Vertical integration of the conservation laws of heat and moisture from the tropopause pressure p_T to the surface pressure p_s yields

$$\langle Q_1 \rangle = \langle Q_R \rangle + LP + S, \quad (1)$$

$$\langle Q_2 \rangle = L(P - E), \quad (2)$$

where $\langle Q_R \rangle$ is the tropospheric net-radiative heating rate, P is precipitation rate, E is evaporation rate, S is sensible heat flux, and $\langle \rangle \equiv 1/g \int_{p_T}^{p_s} (\) dp$. Subtracting (2) from (1) yields

$$\langle Q_R \rangle = \langle Q_1 \rangle - \langle Q_2 \rangle - S - LE. \quad (3)$$

Using these equations, budget-derived estimates of rainfall and tropospheric net-radiative heating rates were computed over the enhanced sounding arrays using the 1° gridded dataset and the JMA/GAME reanalysis surface flux data, which were adjusted toward the flux measurements at the ships with a procedure described in JC02. Because of the difficulty of determining changing cloud fields as a function of time and height (Johnson 1980), hydrometeor storage effects are neglected in this study.²

c. Other data sources

As mentioned above, JMA/GAME V1.1 reanalyses data were used to supplement sonde observations in data-sparse regions and to extend surface flux estimates over the budget networks. This special reanalysis dataset was available for the SCSMEX period over Asian and Pacific regions at 6 h, 0.5° resolution, and 17 vertical levels for upper-level fields, and at 1.25° reso-

lution for surface fields. The JMA/GAME reanalyses used a three-dimensional optimum interpolation scheme for assimilating the standard operational data from this region, as well as data from the enhanced SCSMEX observing network, satellite-derived cloud-drift winds, aircraft reports, and wind profiler observations (Yamazaki et al. 2000).

Satellite data used in this study are from a variety of sources. Estimates of various cirrus (Ci) parameters are from a 6-h, 2.5° global cirrus dataset that was developed from two infrared channels (Luo and Rossow 2004). The advantage of this split-window dataset over the International Satellite Cloud Climatology Project (ISCCP) dataset is that the former analyses provide estimates of cirrus properties at night. Outgoing longwave radiation (OLR) data, which serve as a proxy for deep convection (Liebmann and Smith 1996), were obtained from the National Center for Atmospheric Research (NCAR) on a daily and global basis at 2.5° resolution. Rainfall estimates based on a merged satellite/gauge dataset for the period 1979–2003 were obtained from the Global Precipitation Climatology Project (GPCP; Adler et al. 2003) V2 monthly product at 2.5° resolution. For the May–June 1998 period, rainfall estimates were obtained from the 3-h, 0.25° -resolution TRMM 3B42 version 6 microwave/IR merged rainfall product (Kummerow et al. 2000; Huffman et al. 2005), the daily, 1° GPCP V2 dataset (Huffman et al. 2001), and 6-h, 1.25° values from the JMA/GAME V1.1 reanalysis. SST data were used from the TRMM Microwave Imager (TMI) SST product (Wentz et al. 2000).

3. Flow field and rainfall pattern during SCSMEX

a. Large-scale circulation

The monsoon onset over the SCS is marked by a shift of the low-level wind direction from an easterly to a southwesterly component and typically an increase in rainfall. Depending on the criteria used, the onset date over the SCS for 1998 was determined to be from 15 to 25 May (Ding and Liu 2001; Li and Wu 2000; Chan et al. 2000; Wang et al. 2004). These onset dates are near the climatological average for this region, which is generally accepted to occur in the 28 pentad, or 16–20 May (Tao and Chen 1987; Wang et al. 2004). Regardless of the exact onset date, Ding and Liu (2001) showed a near-simultaneous (within a few days) commencement of the monsoon westerlies over the entire latitudinal range of the SCS during 1998, which is typical for most years (Tao and Chen 1987; Wang et al. 2004). Since the low-level wind shift to southwesterlies occurred near 15 May over both the northern and southern SCS regions,

² A preliminary assessment of hydrometeor storage effects on the diurnal cycle of budgets over the CBA shows that inclusion of these effects due to diurnal changes in cirrus coverage are quite small (i.e., $<0.25 \text{ K day}^{-1}$).

for simplicity the onset date for this study was chosen to be 15 May.³

The transition of the large-scale flow field over the SCS accompanying the 1998 summer monsoon onset is described in Ding and Liu (2001) and JC02. Figure 2 shows the large-scale flow field at three levels (200, 500, and 850 hPa) prior to and after the onset date. Prior to 15 May the SESA region was dominated with low-level easterly flow, while southwesterly flow occurred above 400 hPa. The attendant flow over the NESA during this period was southeasterly at low levels, westerly at midlevels, and strong northwesterly at 200 hPa. Near the time of the onset the flow field quickly transitioned where at low levels the western Pacific subtropical ridge moved eastward, resulting in southwesterly flow at 850 hPa over the entire SCS. At upper levels a strong anticyclone developed over the Tibetan Plateau with an easterly jet on its southern flank centered near the latitudes of the SESA region. The switchover to upper-level easterlies occurred around 15 May over the SESA but considerably later over the NESA (around 10 June).

Several studies have discussed mechanisms responsible for the monsoon onset over the SCS (e.g., Chen and Chen 1995; Chang and Chen 1995) and in particular for 1998 (Chan et al. 2000; Ding and Liu 2001). The latter study showed that the onset process in 1998 began with pair of tropical cyclones during early May that straddled the equator around 80°E. Most likely this cyclone pair was produced from MJO convection, which was present over the equatorial Indian Ocean during this time (see Fig. 3), through a process by which cyclonic potential vorticity anomalies are produced at the poleward edges of an equatorially centered MJO convective envelope (Niето Ferreira et al. 1996). As the NH tropical cyclone moved north and eastward from near Sri Lanka into the Bay of Bengal, it spread deep moisture and southwesterly winds across the northern SCS (Chan et al. 2000).

Over the southern SCS, the flow transition to low-level westerlies near the time of the monsoon onset was accompanied by the passage of a strong equatorial wave that emerged from the MJO convection. Figure 3 shows a time–longitude Hovmöller of OLR for the SCSMEX period averaged between 2.5°S and 2.5°N. As seen in this diagram, as well as the Hovmöller centered farther north over the SESA region (not shown), convection associated with an MJO-like disturbance propagated eastward across the Indian Ocean in early May

with a speed around 5 m s⁻¹. Then around 14 May and near the longitude of the SESA, a separate convective signal emerges and moves more rapidly eastward with a phase speed of 15 m s⁻¹. Based on its speed and the associated changes in the surface wind field as seen in Tropical Atmosphere Ocean Project (TAO) buoy data, Kiladis and Straub (2003) suggest that this latter coherent OLR feature in Fig. 3 is a signature of a convectively coupled Kelvin wave (Straub and Kiladis 2003). Furthermore, this study and Takayabu et al. (1999) have shown that this wave was instrumental in the abrupt termination in May 1998 of a strong El Niño event and the establishment of convection at its more typical longitudes over the Maritime Continent as evidenced by the increase in convective activity after 15 May between 70°E and the date line (Fig. 3).

b. Rainfall distribution

The horizontal distribution of rainfall over the SCSMEX domain for the May–June 1998 period is shown in Fig. 4. Overall, heavier rainfall amounts during this period were located in coastal regions with lighter amounts over oceanic regions. The highest rain rates were centered just inland over southern China near Hong Kong with a band of higher values extending eastward over the NESA toward the southern tip of Taiwan. Other prominent, but smaller, maxima are located near the western Cambodia and Borneo coasts. Rainfall minima are located over the oceans on either side of Borneo and along the east coast of Vietnam extending eastward toward the north coast of Luzon, Philippines.

To put the May–June 1998 rainfall pattern into a longer-term perspective, Fig. 5 shows the May–June 1998 rainfall anomaly distribution from the 25-yr mean (1979–2003). In addition, Fig. 6 shows the annual cycle of GPCP rainfall for the NESA and SESA regions for 1998 and the 25-yr mean. The long-term mean annual cycle shows an increase in rainfall over both regions in spring associated with the summer monsoon onset, with a secondary peak in June and primary peaks in August over the NESA and in November over the SESA. In comparison to the 25-yr mean over this region, the NESA region in May 1998 was 16% wetter while June 1998 was 6% wetter (or overall the 2-month period was 10% wetter). In contrast, the SESA region in May 1998 was 47% drier, while June 1998 was 17% wetter (or overall the 2-month period was 3% drier).

In a recent paper, Lau and Wu (2001) using singular value decomposition (SVD) analysis on a 20-yr record of data have shown that ENSO-related SSTs account for about 30% of the variance of monthly rainfall anomalies over the ASM region as a whole, with this

³ Choosing a later onset date (e.g., 25 May) had no appreciable effect on the results in this study.

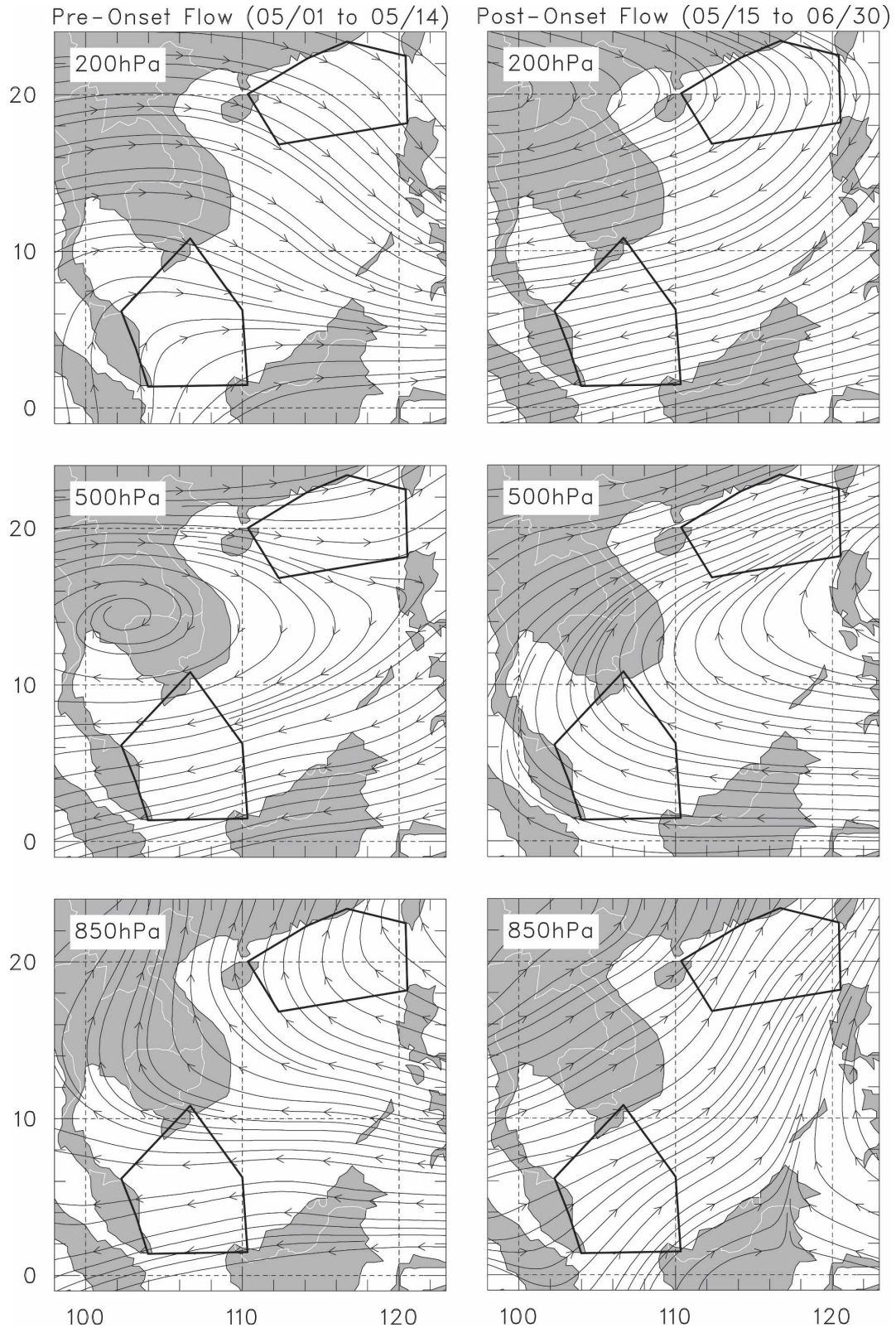


FIG. 2. Streamline analysis at (top) 200, (middle) 500, and (bottom) 850 hPa for the pre-onset (1–14 May) and post-onset (15 May–30 June) periods.

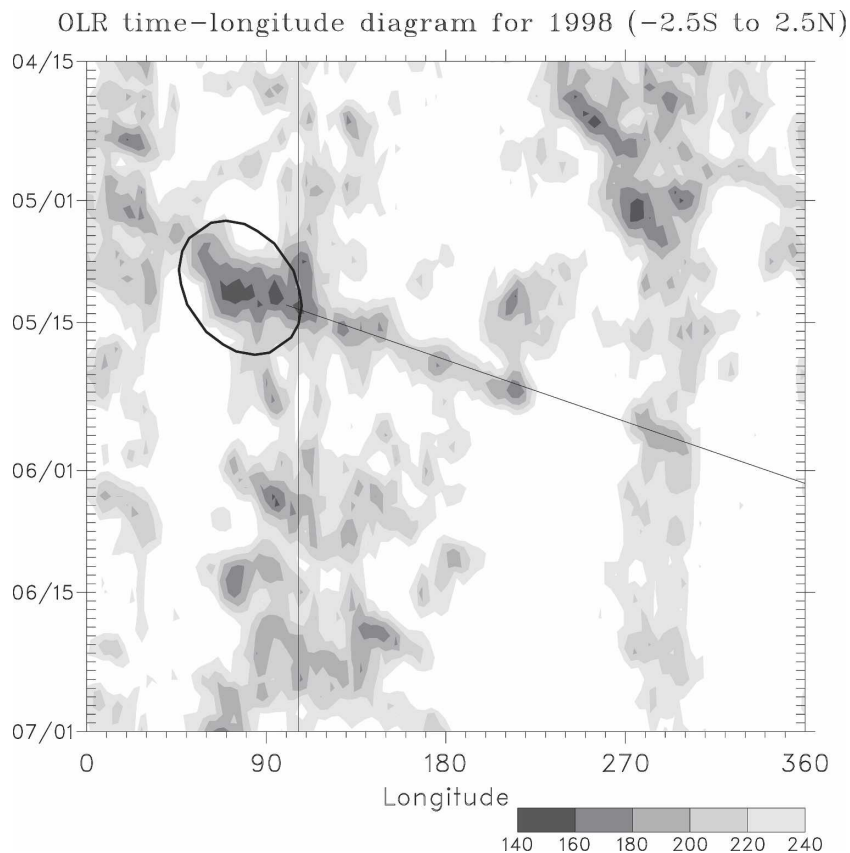


FIG. 3. Longitude–time Hovmöller diagram of OLR (W m^{-1} , with scale at lower right) between 2.5°S and 2.5°N . Vertical line at 105°E indicates central longitude of SESA. Ellipse denotes region of MJO-like convection over the Indian Ocean, while the solid diagonal line marks the progression of the convectively coupled Kelvin wave discussed in the text.

percentage varying in individual years and in subregions. To examine ENSO's impact on the 1998 rainfall pattern over the SCSMEX region, a regression analysis was performed between the May–June Niño-3.4 index and concomitant GPCP monthly rainfall maps for the period 1979–2003 (Fig. 7). As shown in this figure, the rainfall pattern is dominated by positive anomalies along the south China coast and negative anomalies over much of the southern SCS region peaking over the Philippine Islands. A similar pattern was found by Lau and Wu (2001) in the first SVD mode, which they state is part of the ENSO-related basin-scale east–west rainfall dipole with a negative anomaly over the Maritime Continent and a positive anomaly over the central equatorial Pacific. The resemblance between the ENSO rainfall regression map and the May–June 1998 anomaly pattern in Fig. 5 shows that results for this strong ENSO year are consistent with a statistical composite of past ENSO events.

The transition from anomalously dry in May 1998 to

anomalously wet conditions in June over the SESA domain (as seen in Fig. 6) is likely related to the rapid decay of the strong El Niño event during the spring of 1998 and the onset of a strong La Niña (Lau and Wu 2001). The Niño-3.4 index fell from $+2.8$ K in early 1998 to $+0.9$ K in May to -0.7 K in June of this year. Lau and Wu attributed the second SVD mode in their analysis to developing La Niña conditions and claim that this mode had a strong influence on 1998 summertime rainfall anomalies over much of eastern and southern Asia.

4. Atmospheric variability over the SESA domain

Since the characteristics of atmospheric variability over the NESAs domain during SCSMEX were detailed in JC02, this section focuses primarily on the SESA domain. To examine the temporal changes over this region, the 1° gridded fields were averaged over the SESA.

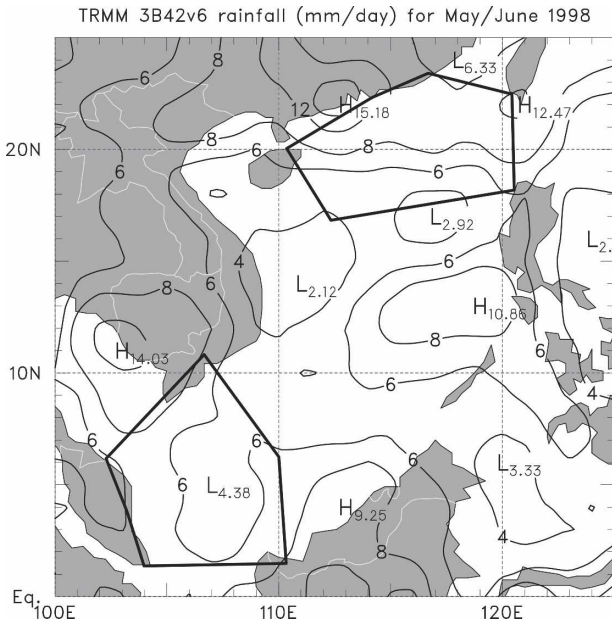


FIG. 4. Horizontal distribution of rainfall for the May-June 1998 period based on the TRMM 3B42V6 product. To remove high-frequency spatial noise from the analysis, the 0.25° data were interpolated onto a 1° grid and a 1-2-1 spatial filter was applied.

a. Surface fields and convective parameters

The temporal relationships among several surface fields, surface fluxes of sensible heat (SH) and latent heat (LH) and OLR are shown for the SESA region in

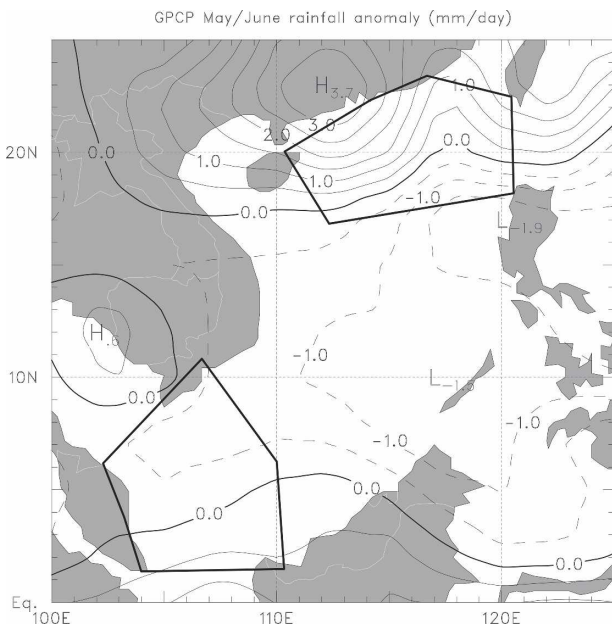


FIG. 5. May-June 1998 rainfall anomaly (from the 25-yr mean) computed from the monthly averaged GPCP rainfall product.

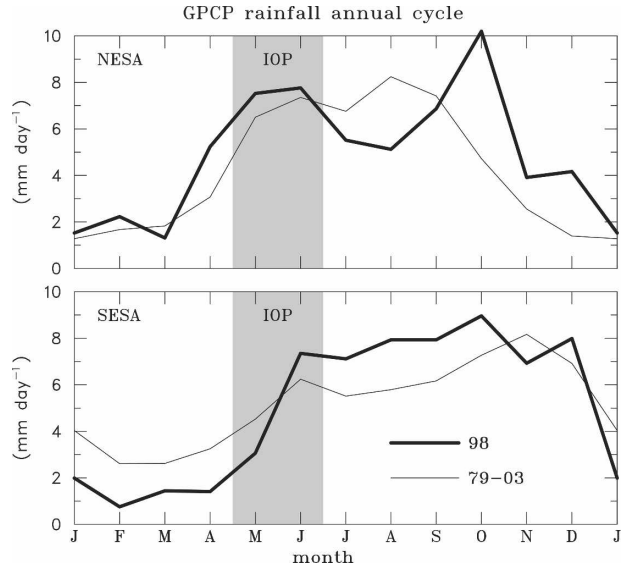


FIG. 6. Annual cycle of rainfall [(top) NESA; (bottom) SESA] for 1998 (heavy line) and 25-yr mean (thin line) computed from the monthly averaged GPCP rainfall product.

Fig. 8. The SESA-averaged SST (top panel) shows little variability during the SCSMEX period, ranging between 30° and 31°C. The coolest SSTs, which occurred around 10 May and 25 June, are related to convectively active periods when wind speeds, surface fluxes, and

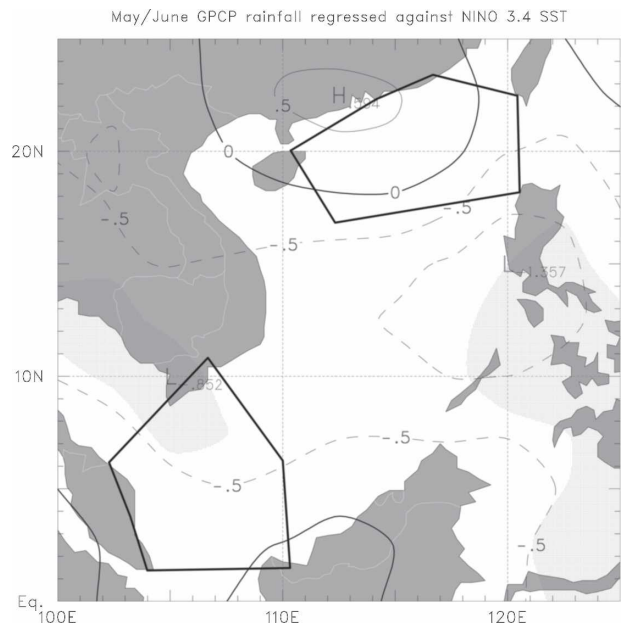


FIG. 7. Regression coefficient map (mm day⁻¹ per std dev Niño-3.4 index) between May-June GPCP monthly rainfall and the standardized Niño-3.4 index. The stippling indicates areas where the regression coefficients are significant at the 95% confidence level based on a two-tail Student's *t* test assuming 25 degrees of freedom.

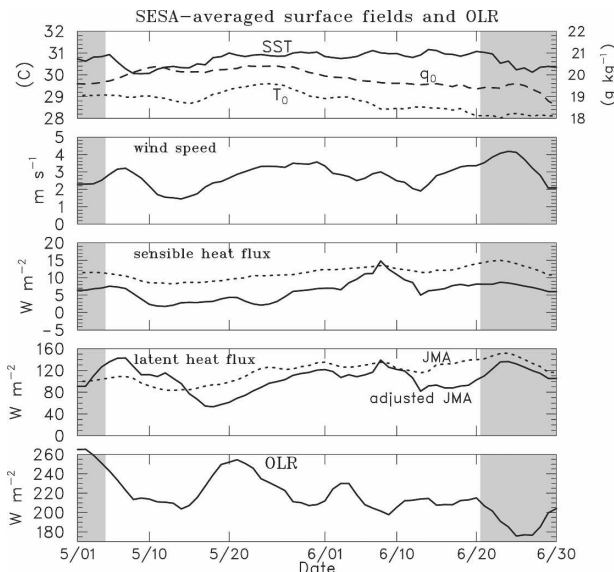


FIG. 8. Time series of filtered (5-day running mean) surface fields and OLR averaged over the SESA. (top) SST (solid curve), surface temperature T_o (dotted curve) with scale to left and specific humidity q_o (dashed) with scale to right. (second) Surface wind speed. Adjusted (solid curves) and unadjusted (dotted curves) JMA/GAME reanalysis (third) sensible and (fourth) latent heat fluxes. Adjusted values are based on bulk flux measurements from *Kexue #1*. (bottom) OLR. Shaded times are outside SCSMEX IOP.

rainfall (inferred from the low OLR values during these periods) are enhanced. The SESA-averaged surface specific humidity, and temperature (top panel of Fig. 8) reached their peak values around 25 May, which was near the end of a quiescent period when convective activity was low (high OLR values in Fig. 8). After this date a slow cooling and drying trend in the surface fields led to a gradual increase in the surface fluxes. The dependence of surface fluxes on wind speed is readily seen in Fig. 8 with enhanced fluxes occurring during periods of stronger surface winds, which generally developed prior to and during convectively active periods. While the surface winds speeds ($|\mathbf{u}|_o$) were about 25% lighter over the SESA compared to the NESAs (Table 1), surface fluxes were more than double over the SESA due to larger air–sea temperature and moisture differences in this region. As noted in JC02, advection of warm, moist air over the cooler waters of the NESAs substantially reduced the surface fluxes in that region after the monsoon onset. The low-level flow field shown by the post-onset 850-hPa streamline pattern in Fig. 2 suggests that the ample surface fluxes over the SESA likely contributed to the source of warm, moist air that was advected over the NESAs region. The magnitude of the May–June 1998 SESA-averaged surface fluxes (112 W m^{-2}) is similar to that observed over the

TABLE 1. May–June 1998 averaged quantities over the NESAs and SESA domains. Here Ci refers to cirrus and Cs to cirrostratus clouds.

Quantity	Units	NESAs	SESA
Rainfall (GPCP 1°, daily)	mm day ⁻¹	7.6	4.9
Rainfall (TRMM 3B42V6)	mm day ⁻¹	7.4	5.8
Rainfall (Q_2 budget)	mm day ⁻¹	5.7	5.3
$ \mathbf{u} _o$	m s ⁻¹	3.6	2.8
Latent heat flux	W m ⁻²	41.7	105.3
Sensible heat flux	W m ⁻²	2.4	6.3
$\langle Q_T \rangle$	K day ⁻¹	-1.11	-0.47
Cirrus (Ci + Cs) cloud fraction	%	48	54
Cs cloud top	hPa	270	253

intensive flux array (IFA) in the 1992–93 Tropical Ocean Global Atmosphere Coupled Ocean–Atmosphere Response Experiment (TOGACOARE) (115 W m^{-2} ; Johnson and Ciesielski 2000).

The temporal relationship between OLR (i.e., convective activity) and several SESA-averaged convective parameters can be seen from Figs. 8 and 9. Peak values in several of these parameters were attained during the active convective (low OLR) period in mid-May. For example, during this period convective inhibition (CIN) reached a minimum of -67 J kg^{-1} , the level of neutral buoyancy (LNB) was at its highest (118 hPa), and precipitable water (PW) attained a 2-month maximum value of $\sim 6 \text{ cm}$. After the mid-May active period the relationship of these parameters to OLR is less clear. Peak CAPE values are nearly 180° out of phase with convectively active (low OLR) periods. With the onset

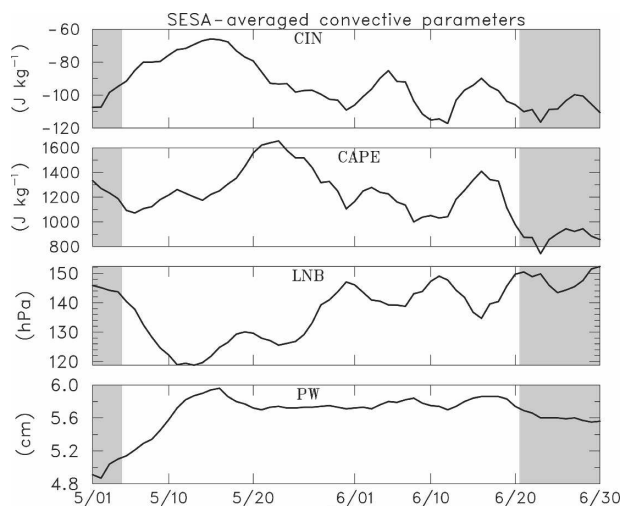


FIG. 9. Time series of filtered (5-day running mean) SESA-averaged convective parameters for the May–June period: (top) CIN, (second) convective available potential energy (CAPE), (third) LNB, and (bottom) PW.

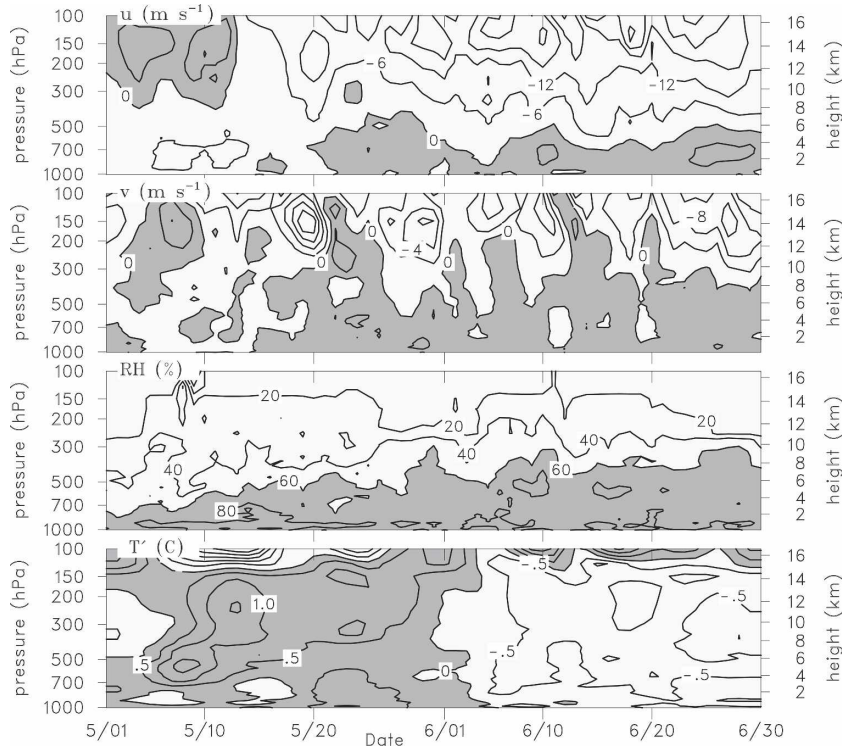


FIG. 10. Time series of filtered (5-day running mean) SESA-averaged u , v , RH with respect to water, and perturbation temperature T' for the May–June 1998 period. Positive wind values, RH value $>60\%$, and positive perturbation temperatures are shaded. Here the perturbation temperature is the deviation from the May–June mean. Contour interval is 6 m s^{-1} for u , 4 m s^{-1} for v , 20% for RH, and 0.5 K for T' .

of deep convection the surface temperature falls (Fig. 8) and CAPE is quickly depleted as observed over the NESAs (JC02) and in the eastern tropical Atlantic (Thompson et al. 1979). Consistent with the high LNB during mid-May, analysis of tropopause heights at R/V *Kexue #1* show anomalously high values of 85 hPa where the two-cruise ship mean was ~ 95 hPa. The cold anomaly seen in SESA perturbation temperatures (Fig. 10) near 100 hPa during this period is a reflection of this high tropopause. After the steady increase of PW through mid-May, it remained relatively constant around 5.8 cm thereafter. While the SESA-mean CAPE value for the SCSMEX period (1200 J kg^{-1}) compares favorably to the mean for TOGA COARE (1272 J kg^{-1}) determined with similar Vaisala RS80-type sondes (Ciesielski et al. 2003), the SESA-mean CIN value (-94 J kg^{-1}) is about double the TOGA COARE value (-43 J kg^{-1}).

b. Upper-level fields of basic and diagnosed quantities

Time series of u , v , relative humidity (RH), and perturbation temperature (T' , deviation from the 2-month

mean) averaged over the SESA domain for the May–June period are shown in Fig. 10. The rapid transition from low-level easterly flow to southwesterly flow around mid-May, associated with the passage of a convectively coupled Kelvin wave (Kiladis and Straub 2003), is clearly seen in these time series. Also related to this wave passage, the flow at upper levels transitions from westerlies in early May to easterlies for the remainder of the SCSMEX period. These dramatic circulation changes can also be seen in Fig. 11, which shows the SESA-averaged vertical profiles of u , v , and RH for the pre-onset (1–14 May) and post-onset (15 May–30 June) periods. Variability in the upper-level post-onset easterlies (Fig. 10) is related to fluctuations in the strength and position of the upper-level anticyclone centered over Tibetan Plateau (Fig. 2) and to the passage of equatorial disturbances. Moreover, fluctuations in upper-level meridional winds around 20 May show evidence for the passage of a mixed-Rossby gravity wave. As discussed in JC02, the westward tilt of the meridional winds with height suggests an upward wave energy flux (Yanai and Hayashi 1969) associated with this wave, which moved westward at $\sim 16 \text{ m s}^{-1}$ and had

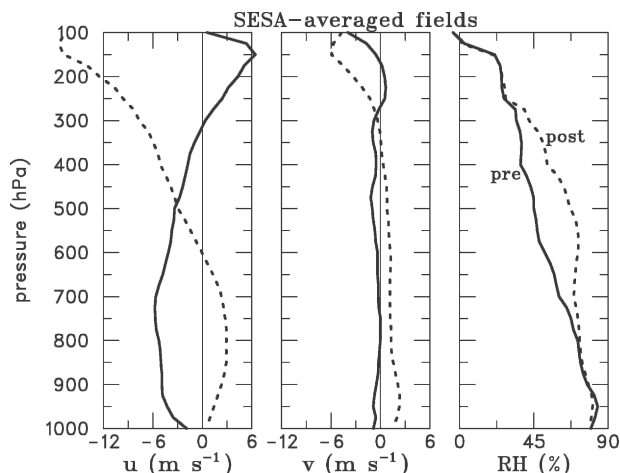


FIG. 11. SESA-averaged vertical profiles of u , v , and RH with respect to water, for the pre-onset (1–14 May; solid curves) and post-onset (15 May–30 June; dashed curves) periods.

a wavelength of ~ 5000 km. Similar, but somewhat weaker, signatures are present in the upper-level meridional winds around 10 June and again near the end of June.

The relative humidity time series (third panel of Fig. 10) shows a low-level moist layer that gradually deepens as the monsoon progresses. For example, near the beginning of May the layer of 60% and greater RH was confined below 700 hPa (Fig. 11) but by late June this moist layer extended up to 300 hPa. During the SCS-MEX period the SESA-averaged T' field (bottom panel of Fig. 10) exhibited a notable cooling trend, particularly at upper levels where 200-hPa temperature decreased by about 3°C between 13 May and 18 June. The deepening moisture field and cooling aloft as the monsoon progressed contributed to periods of the increased instability and convective activity (see CAPE and OLR in Figs. 8 and 9) over the SESA domain.

The temperature perturbations during the pre-onset period seen in Fig. 10 are quite striking, in particular, the warm perturbations (>1.5 K) around 8 May near 600 hPa and on 13 May near 250 hPa. Johnson and Ciesielski (2000) found warm anomalies of a similar magnitude centered near 300 hPa in TOGA COARE (see their Fig. 12). These anomalies occurred during periods with high cirrus coverage and heavy rainfall and are presumably a response to latent and radiative heating, although the precise mechanisms were not identified. A clue to the mechanisms generating the upper-level warm anomaly in Fig. 10 can be found by noting that its peak amplitude is coincident with low OLR (Figs. 3 and 8), which is associated with passage of a convectively coupled Kelvin wave during the 1998 sum-

mer monsoon onset. Using a regression analysis of OLR data with multiple years of ECMWF reanalysis and station radiosonde data, Straub and Kiladis (2003) found warm over cold anomalies in the low OLR region associated with convectively coupled Kelvin waves. They suggest that this second baroclinic mode structure (i.e., warm over cold anomalies) is indicative of the important role that stratiform precipitation is playing in determining the large-scale wave structure. Also during the mid-May period, the cirrus cloud fraction over the SESA was quite high (as shown in the next section in Fig. 15), which likely contributed to the warming by decreasing the longwave emission from the atmosphere and enhancing shortwave heating within the cirrus cloud layer (Randall et al. 1989).

Time series of diagnosed quantities (divergence, vertical motion, Q_1 , and Q_2) averaged over the SESA domain are shown in Fig. 12. In contrast to conditions over the NESAs, which had two extended periods (7–10 days) of deep convection during May and June (JC02), the SESA domain was characterized by more frequent but weaker convective episodes (see rainfall time series in Fig. 13). During the convectively active periods over the SESA, upper-level divergence typically peaked around 150 hPa or higher. Prior to the passage of the convectively coupled Kelvin wave around 15 May, convergence peaked near the surface, while after this date divergence was observed near the surface with an elevated convergence layer peaking near 700 hPa and occasionally extending to midlevels (i.e., ~ 500 hPa). As a result of this vertical divergence structure, periods with significant upward vertical motion after mid-May exhibited weak subsidence in the lowest layers. In their study of Doppler radar–derived divergence profiles in 10 mesoscale convective systems (MCSs) in TOGA COARE, Mapes and Houze (1995) showed that divergence profiles with elevated convergence and surface divergence characterize older precipitating cells with well-developed downdrafts. Furthermore, their results indicate that midlevel convergence is generally associated with stratiform precipitation, which is common in the decaying stages of MCSs. As will be shown in section 6, much of the convection over the SESA occurs as decaying westward-propagating systems that formed in the early morning hours off the northwest coast of Borneo. Consistent with this idea, the upper-level positive peaks of Q_1 and Q_2 (i.e., heating and drying) after mid-May had attendant layers of negative values (i.e., cooling and moistening) in the lowest few kilometers, indicative of rainfall evaporation as would occur in older raining cells or decaying MCSs.

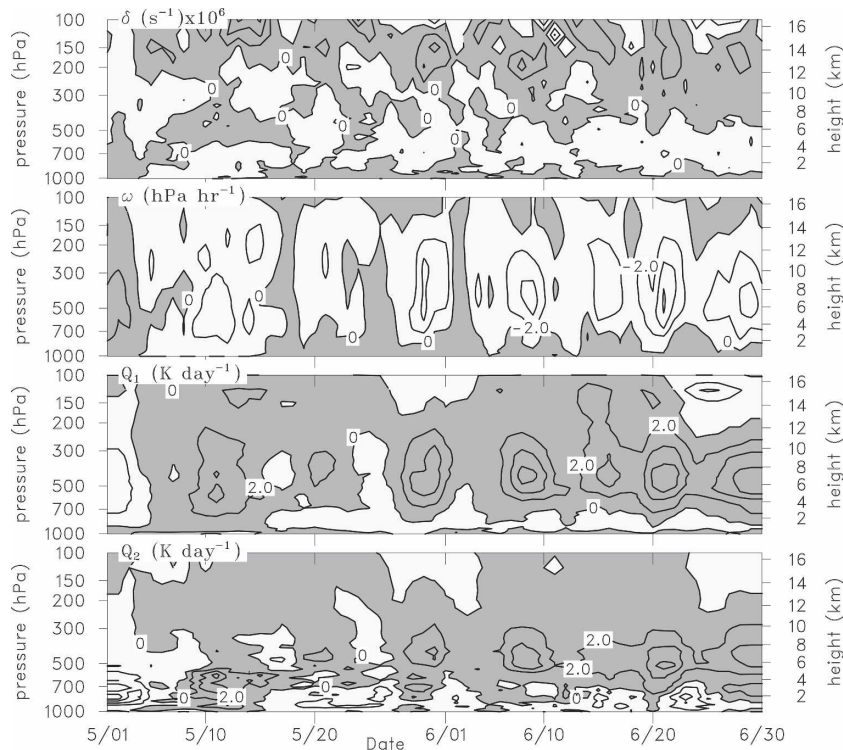


FIG. 12. Time series of filtered (5-day running mean) SESA-averaged divergence, vertical motion, Q_1 , and Q_2 for the May–June 1998 period. Positive values in each field are shaded. Contour interval is $6 \times 10^{-6} \text{ s}^{-1}$ for divergence, 2 hPa h^{-1} for vertical motion, and 2 K day^{-1} for Q_1 and Q_2 .

5. Comparison of NESA- and SESA-averaged fields

a. Rainfall time series

Time series of various daily rainfall estimates over the enhanced sounding networks are shown in Fig. 13. The budget-derived rainfall estimates presented here were computed using (2) with details provided in section 2. The NESA time series (top panel) shows two ~ 10 day rainy periods separated by a weeklong break near the end of May. Fukutomi and Yasunari (1999) found that fluctuations of convection on this time scale (10–25 days) over the SCS were related to circulation patterns covering large regions of the Asian–Pacific sector. Overall, there is good agreement between the budget-derived rainfall and other estimates over the NESA region. This is particularly true for the 47-day IOP (nonshaded portion of Fig. 13 in which the sonde data coverage was most complete) during which time the correlation between the filtered (5-day running mean) TRMM and budget-derived daily rainfall time series was 0.95. The satellite-based GPCP rain rates agreed well with the other estimates except during the second rainy period when its rates were too low. The

JMA/GAME reanalysis estimates tended to be slightly high throughout the 2-month period.

Over the SESA domain (lower panel of Fig. 13), the rainfall time series show a rainy period associated with the passage of the convectively coupled Kelvin wave in mid-May, followed by a weeklong break and then several episodic rain events with increasingly higher rain rates. Once again the budget and satellite estimates agree reasonably well during the IOP. For example, the IOP mean for TRMM is 4.5 mm day^{-1} compared to 5.4 mm day^{-1} for the budgets, with a correlation between the filtered IOP time series of 0.79. This good agreement indicates that the enhanced sounding network did a reasonable job of capturing the large-scale vertical motion field over the southern SCS. Outside the IOP (i.e., the shaded region of these plots when ships were not present and most sites had only two sondes per day), the budget estimates in both regions compare quite poorly to the satellite estimates. The higher correlation between the budget and TRMM rainfall estimates over the NESA (0.95) compared to the SESA (0.79) is probably due to a higher frequency of TRMM overpasses over the NESA as well as better sonde coverage in this northern region (Fig. 1). For reasons that

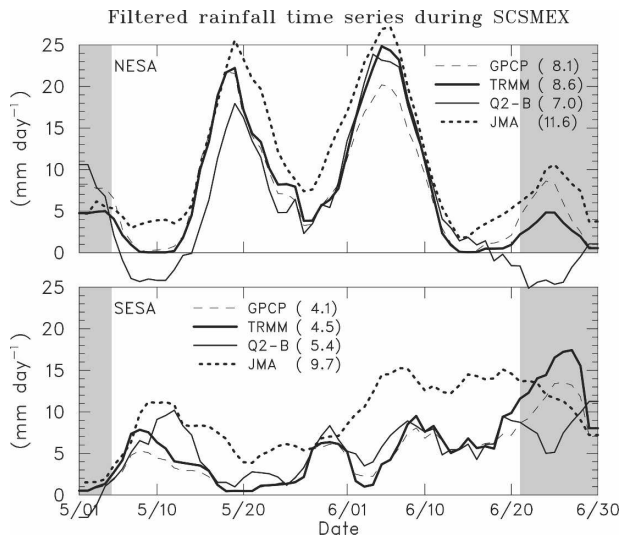


FIG. 13. Time series of various filtered (5-day running mean) rainfall estimates for the May–June 1998 period averaged over the (top) NESAs and (bottom) SESA. Estimates are from daily GPCP product (dashed curves), TRMM 3B42V6 product (heavy solid curves), moisture (Q_2) budget (thin solid curves), and JMA/GAME reanalysis (dotted curves). IOP-mean values are in parentheses. Shaded times are outside SCSMEX IOP.

are unclear, the JMA/GAME rain rates over the SESA are considerably higher than the other estimates throughout most of the period.

Figure 13 also shows a tendency for the rainfall time series to be anticorrelated between the two regions (e.g., the correlation between the NESAs and SESA TRMM IOP daily time series is -0.47). This compensation between the rainfall in these two regions may be related to fluctuations in the Hadley circulation such that a more intense Hadley cell would result in stronger rising motion near the equator and greater subsidence in the subtropics. An alternate explanation may be related to the analyses of Nitta (1987), Chen and Chen (1995), and Lawrence and Webster (2002) who found that northward-migrating intraseasonal modes caused alternating north–south patterns in rainfall over the south Asian summer monsoon region. The basis for Nitta’s analysis were alternating OLR anomalies over the western Pacific (the so-called Pacific–Japan pattern), which he attributed to Rossby wave trains emanating from tropical heat source regions. Related to these studies, Chan et al. (2002) found that intraseasonal variability in convective activity during the SCSMEX period was controlled mainly by a northward-propagating 30–60-day mode. This oscillation was detected as an east–west elongated trough/ridge pattern associated with bands of active and suppressed convection that moved northward from the equator over the SCS.

b. Vertical profiles of diagnosed quantities

Vertical profiles of divergence, vertical motion, Q_1 , Q_2 , and the vertical eddy heat flux (F) averaged over the NESAs and SESA domains for periods of appreciable rainfall during the SCSMEX IOP are shown in Fig. 14. Based on the rainfall time series in Fig. 13, the 37-day period from 15 May⁴ to 20 June was chosen for the NESAs analyses, whereas the entire 47-day IOP from 5 May to 20 June was chosen for the SESA analyses. Here F is defined as

$$F \equiv -\frac{\overline{h'\omega'}}{g} = S + LE + \frac{1}{g} \int_{p_s}^p (Q_1 - Q_2 - Q_R) dp, \quad (4)$$

where $h = c_p T + Lq + gz$ is the moist static energy. At the surface, F is computed from the JMA/GAME reanalysis fluxes that have been adjusted toward the ship values (i.e., $F_0 = S + LE$). Above the surface, the procedure used here for computing F assumes a constant Q_R (since its vertical profile is unknown) such that $F = 0$ at 100 hPa. The average values of Q_R that give $F = 0$ for the periods in questions are -1.17 and -0.46 K day^{-1} for the NESAs and SESA, respectively. These values differ only slightly from the May–June mean values of Q_R listed in Table 1.

While the large cooling rate observed over the NESAs is somewhat suspicious, as discussed in JC02, the value of $\langle Q_R \rangle$ over the SESA seems quite reasonable and compares favorably to that observed over the western Pacific warm pool during TOGA COARE (-0.55 K day^{-1} as reported in Ciesielski et al. 2003). Johnson and Ciesielski (2000) suggested that this small cooling rate during TOGA COARE was related to decreased long-wave emission due to abundance of cirrus clouds (55% coverage) over the warm pool. Some support for these findings is seen in the greater high-cloud fraction over the SESA compared to the NESAs (see Table 1). However comparison of $\langle Q_R \rangle$ and high-cloud-fraction time series over these regions (not shown) reveal little, if any, correlation suggesting that other factors (e.g., the complete cloud field including subvisible cirrus, temperature, and water vapor distributions) are playing an important role in the determination of $\langle Q_R \rangle$. Regardless of the reasons, the large differential radiative heating rates between the NESAs and SESA could have important implications for understanding the dynamics of the SCS region. For example, Raymond (2000) has postu-

⁴ Very little rain was observed over the NESAs prior to the monsoon onset in mid-May.

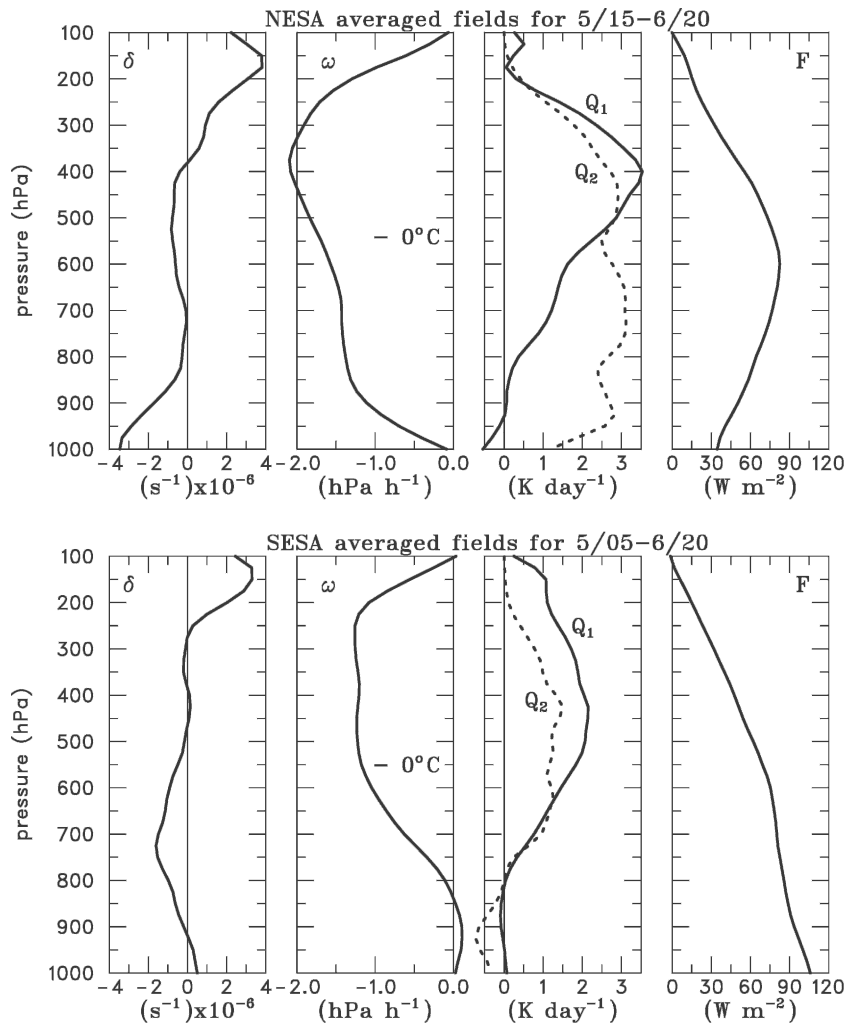


FIG. 14. Vertical profiles of divergence, vertical motion, Q_1 (solid curve) and Q_2 (dashed curve), and vertical eddy heat flux F averaged over convectively active periods in the (top) NESA and (bottom) SESA.

lated that latitudinal radiative differences play an important role in the dynamics of the Hadley circulation.

Vertical profiles of diagnosed fields averaged over the NESA are shown in the top panel of Fig. 14. The NESA-averaged divergence profile is characterized by strong low-level convergence with an upper-level divergence peak around 150 hPa. The vertical motion profile has a broad low-level peak around 800 hPa with a stronger upper-level peak (~ 2 hPa h^{-1}) near 375 hPa. JC02 note that this upper-level peak may reflect a contribution from stratiform rain in this region. Johnson et al. (2005) have shown from a ground-based radar analysis that during the onset convective period from 15 to 25 May the fraction of stratiform rainfall near Dongsha Island within the NESA was rather small (26%) compared to values around 40%, which are typically ob-

served in the Tropics (Schumacher and Houze 2003). Unfortunately, the stratiform rain fraction during the June rainy period could not be determined due to unreliable radar data. The mean profiles of Q_1 and Q_2 (their magnitude and the vertical separation between their peaks) are indicative of deep convection (Luo and Yanai 1984), with the shape of the Q_1 profile similar to those found in earlier studies over the tropical western Pacific (Yanai et al. 1973) and eastern Atlantic (Thompson et al. 1979). This conclusion of a high convective fraction over the NESA is supported by the vertical profile of F , which increases rapidly with height from a small surface flux value of 37 $W m^{-2}$ and has a broad peak at midlevels.

For comparison, the IOP-mean vertical profiles of the diagnosed fields averaged over the SESA domain

are shown in bottom panel of Fig. 14. Consistent with smaller rain rates over the SESA (Fig. 13; Table 1), the ω , Q_1 , and Q_2 peaks are noticeably smaller than those observed over the NESAs. The mean divergence profile shows weak surface divergence, an elevated low-level convergence peak around 700 hPa, and an upper-level divergence peak around 125 mb. This higher outflow level over SESA is consistent with higher cloud tops (Table 1) and the higher tropopause observed there. Analysis of tropopause heights from the ship sonde data indicates a mean tropopause height about 5–10 hPa higher at the southern ship. The divergence profile results in weak low-level subsidence with an elevated peak in rising motion. This along with the negligible vertical separation in the Q_1 and Q_2 peaks and the presence of low-level moistening and cooling suggests that the SESA stratiform rain fraction is quite significant and larger than that observed over the NESAs.

The SESA IOP-mean profile of F in Fig. 14 decreases steadily with height from its large surface value of 108 W m^{-2} and above 700 hPa is less than its counterpart NESAs profile. Since F arises primarily from convective areas where vertical motions and eddy fluxes are largest (Johnson and Young 1983; Yanai and Johnson 1993), the large values of F below 700 hPa imply, along with deep convection, a significant presence of shallow precipitating clouds in this region. A similar conclusion of a ubiquitous shallow-convective heating field in the Tropics was reached by Mapes (2000) based on a mismatch between profiles of radiative cooling and net heating in regions of concentrated deep convection. In addition, cloud photos and weather logs taken at the R/V *Kexue #1* during its first cruise (M. Garcia 1998, personal communication) corroborate the notion that a significant trade cumulus and precipitating congestus population was present in the SESA region. With such a precipitating congestus population one would expect to find an attendant low-level heating and drying signature in the mean Q_1 and Q_2 profiles. The absence of this shallow-cloud signal in the SESA mean profiles (Fig. 14) leads us to speculate that it is being masked in this area- and time-averaged result by the cooling and moistening effects at low levels of a large stratiform rain fraction.

c. Upper-level cloudiness

Time series of upper-level cloud fraction for the NESAs (top panel) and SESA (bottom panel) are shown in Fig. 15. The definitions for cirrus (Ci) and cirrostratus (Cs) clouds follow the classification scheme used in the ISCCP D-series dataset where cloud-top pressure is above 440 hPa for both cloud types and optical thickness is less than 3.6 for Ci and between 3.6

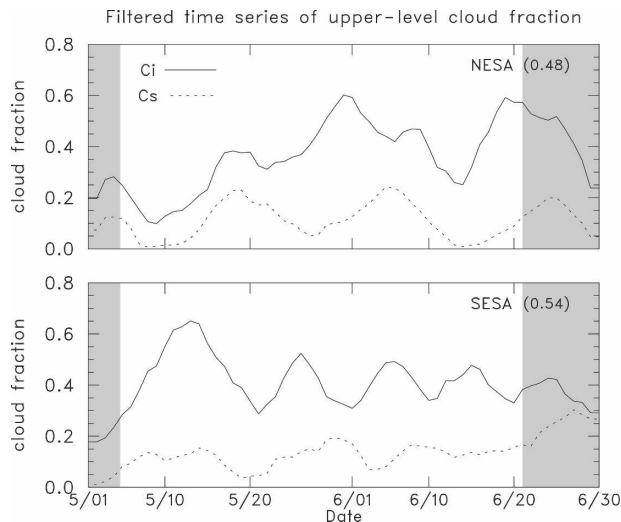


FIG. 15. Time series of filtered (5-day running mean) upper-level cloud fraction estimates from the split-window cirrus dataset (Ci refers to cirrus and Cs to cirrostratus). May–June mean values for Ci + Cs fractions are in parentheses. Shaded times are outside SCSMEX IOP.

and 23 for Cs. As noted in Table 1, the SESA has a 6% higher coverage from upper-level clouds (Ci + Cs). While fairly high Ci coverage is present during the rainy periods over the NESAs, the two highest peaks in Ci coverage occur during relatively suppressed periods (see Fig. 13). During these suppressed periods some of the cirrus over the NESAs may have originated from convection along the south coast of China. Over the SESA the highest Ci fraction occurs during the mid-May convectively active period. Comparing the Cs time series to that of OLR shows high anticorrelations of -0.94 for the NESAs and -0.89 for the SESA. Correlations between Ci and OLR are considerably smaller (-0.67 and -0.37 for the NESAs and SESA, respectively). The sense of these relationships agrees with the observation by Luo and Rossow (2004) that deep convection is followed by immediate growth of Cs and Ci clouds followed by a decay of Cs and continued growth of Ci. Their study also shows that more than half of tropical cirrus are only loosely, if at all, connected to convection, which is consistent with the weaker relationship between Ci and OLR found here.

6. Diurnal cycle of convection over the SCS

Houze et al. (1981) and Ichikawa and Yasunari (2004) have shown that low-level prevailing winds are a crucial factor in modulating the diurnal cycle of convection over the southern SCS region. In view of this finding, this section focuses on the diurnal cycle of rain-

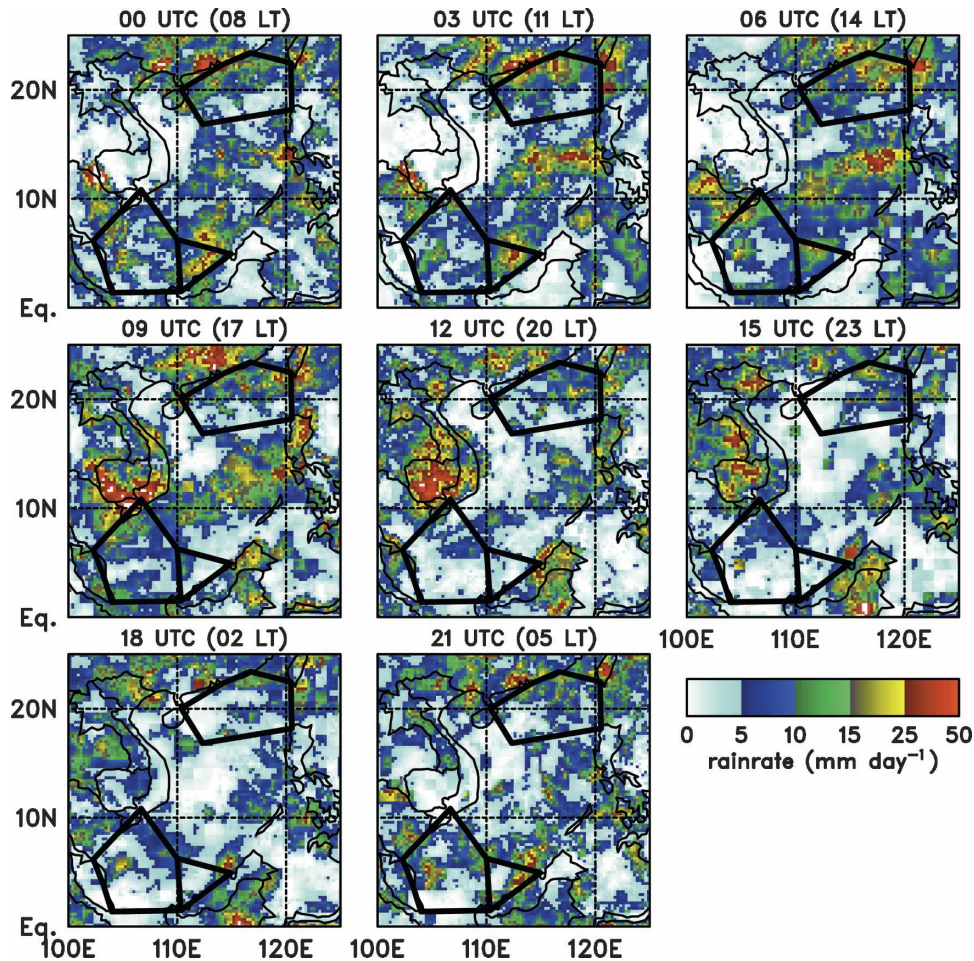


FIG. 16. Three-hourly TRMM 3B42V6 rainfall maps (scale on lower right) averaged over the post-onset SCSMEX period (15 May–30 Jun 1998).

fall over the SCSMEX domain during the post-onset period when low-level southwesterlies predominated over the SCS region. As depicted in Fig. 16, the diurnal cycle of rainfall exhibits several prominent signals over the SCS region. These 3-h rainfall maps were constructed from the 0.25° resolution TRMM 3B42V6 dataset. The characteristics of diurnal convection reported in this section for the 1998 post-onset period are robust in that they consistently appear in other years during this period (analyses not shown).

a. Diurnal rainfall analyses over the NESAs and SESA

Over the NESAs region, the rainfall maps in Fig. 16 show strong early morning convection being initiated along the south China coast. During the course of the day this convection gradually dissipates as it moves south and eastward over the NESAs region. During the onset rainy period over the NESAs from 15 to 25 May

1998, Johnson et al. (2004) using radar and satellite data documented that the early morning coastal convection, which they attribute to the land-breeze convergence with the prevailing low-level flow, propagated away from the coast at about 15 m s^{-1} and underwent a convective to stratiform transition. For the post-onset period the NESAs-averaged rainfall has a diurnal peak near 15 mm day^{-1} at 1400 LT with a minimum of 8 mm day^{-1} at 0200 LT (Fig. 17, top panel).

Convection over the southern SCS also exhibits a strong diurnal signal with several noteworthy features. During the hours from 1700 to 0200 LT, convection is quite strong over the land areas of Malaysia and Borneo, while the adjacent oceanic regions are suppressed (Fig. 16). Around 0500 LT heavy-rainfall-producing MCSs form off the west coast of Borneo as the nighttime land breeze from Borneo converges with the low-level southwesterlies. These systems peak near 0800 LT then gradually dissipate as they propagate

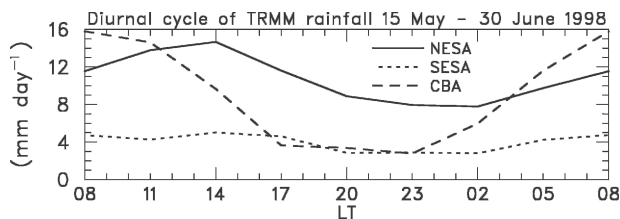


FIG. 17. Diurnal cycle of rain rates from the TRMM 3B42V6 analysis for the post-onset period (15 May–30 June) averaged over the NESAs (solid curve), the SESA (dotted curve), and the CBA (dashed curve).

westward over the SESA during the early afternoon hours. This low-level convergence mechanism is similar to that reported in Houze et al. (1981) for the initiation of MCSs during the 1978 winter MONEX. While Fig. 17 shows a strong diurnal rainfall peak at 0800 LT over the CBA, a broad and weak peak is observed during the early afternoon hours (1400 LT) over the SESA.

b. Diurnal rainfall and budget analyses over the CBA

To examine the characteristics of the post-onset, coastal Borneo convection in more detail, Fig. 18 shows the diurnal cycle of rainfall as a function of longitude for the period from 15 May to 20 June.⁵ In this analysis TRMM rainfall estimates have been averaged in the latitude belt from 3° to 6°N, which covers the CBA and the southern portion of the SESA. From this diagram it appears that the nighttime convection over Borneo (denoted with slanted solid line) propagates westward at about the speed of the steering-level flow (4 m s^{-1}), and then reintensifies off the west coast of Borneo during the early morning hours. The steering flow is taken to be the 400–600-hPa layer-mean wind (Carbone et al. 2002) during this period (Fig. 11). After the mesoscale systems reach their peak intensity between 0500 and 0800 LT, they propagate westward (denoted with slanted dashed line in Fig. 18) to 110°E at about 13 m s^{-1} , which suggests cold pool dynamics or gravity wave mechanisms may be playing a role (Mapes et al. 2003). By early afternoon (1400 LT) rainfall appears to spread rapidly westward across the SESA (i.e., west of 110°E), which likely reflects remnant stratiform anvils that are advected westward by strong upper-level easterly flow (Fig. 11). Using solely TRMM Precipitation Radar (PR) data, Mori et al. (2004) observed a similar

rapid westward spreading of convection southwest of the Sumatra, Indonesia, coastline.

Since the sounding sites in the CBA had good diurnal coverage during the post-onset IOP, vertical profiles of diagnosed fields (ω , Q_1 , and Q_2) composited at the four sonde times are shown for the CBA in Fig. 19.⁶ As one might expect based on the 0800 LT rainfall peak over this region, the profiles at this time show the strongest vertical motion as well as heating and drying effects indicative of strong and deep convective systems. Moreover, the large vertical motions at upper levels and the similarity in the Q_1 and Q_2 profiles suggest that a significant fraction of the convection at this time is stratiform in nature. In a study of the diurnal variations in convection around Sumatra using TRMM PR data, Mori et al. (2004) found that evening rainfall over land was predominately convective in nature, while morning coastal rainfall was composed almost equally of stratiform and convective rain. At 1400 LT the profiles are characterized by decaying stratiform anvils with weak upward vertical motion above the freezing level and subsidence, cooling, and moistening predominating below. The lack of drying above the freezing level in the Q_2 profile at this time would suggest that the attendant upper-level heating is related more to radiative than convective effects. In diurnally forced 1D general circulation model (GCM) simulations with radiative–convective interactions, Randall et al. (1991) found total atmospheric cloud radiative heating rates of $1\text{--}2 \text{ K day}^{-1}$ near local noon. This radiative forcing, which peaks near 12 km ($\sim 225 \text{ hPa}$), is primarily the result of shortwave heating within cumulonimbus anvil clouds (Randall et al. 1989). At 2000 and 0200 LT the vertical motion and budget profiles are indicative of weaker convection consistent with the smaller TRMM rain rates observed over the CBA during these nighttime hours (Fig. 17).

7. Summary and concluding remarks

An important objective of SCSMEX was the establishment of two enhanced sounding networks over the SCS to determine and contrast the properties of convection in two distinct oceanic regions. An earlier study (JC02) focused on analysis over the northern SCS. This study extends this earlier work by examining the cir-

⁵ This corresponds to the period when low-level southwesterlies predominated over the SESA and sounding data coverage in the CBA was most complete.

⁶ The budget profiles (in Fig. 19) below 900 hPa should be regarded with caution because diurnal surface heating effects at the Borneo land sites are aliased onto larger-scale fields by the objective analysis scheme and overwhelm the weaker, low-level, diurnal signal over the ocean.

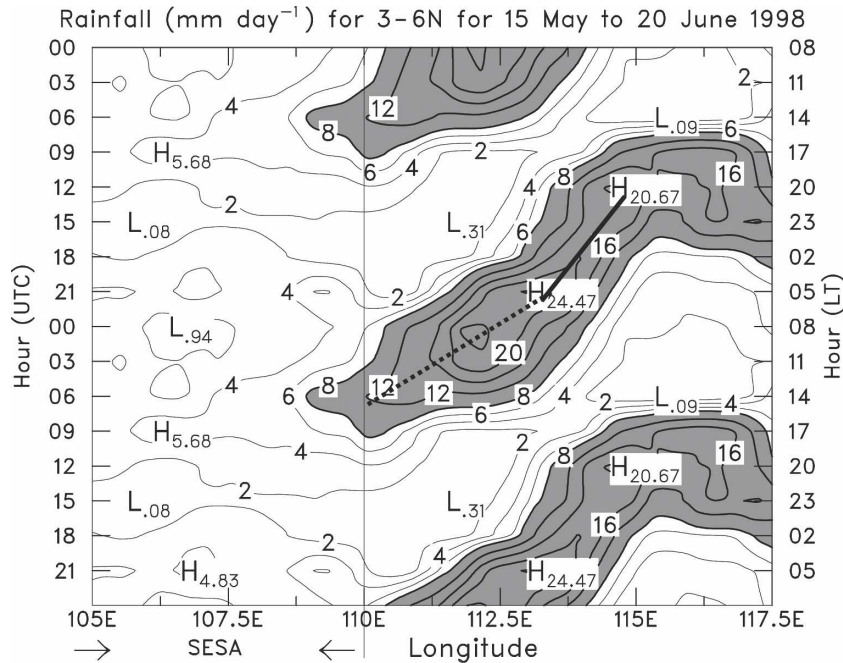


FIG. 18. Time of day vs longitude plot for rainfall averaged over day vs longitude plot for rainfall averaged over the latitude strip from 3° to 6°N. The TRMM 3B42V6 data used in constructing this diagram were for the period 15 May–20 Jun 1998. Contour interval is 2 mm day^{-1} in nonshaded region, and 4 mm day^{-1} in shaded region (i.e., rates above 8 mm day^{-1}). The thin vertical line along 110°E denotes the eastern boundary of the SESA. The slanted solid and dashed lines denote the westward motion of convection with speeds of 4 and 13 m s^{-1} , respectively.

lation and properties of convection over the southern SCS. A comparison of several May–June 1998 quantities averaged over the NESAs and SESAs domains is given in Table 1. The main results of this study are summarized below.

The monsoon onset over the SESA around mid-May coincided with the passage of a convectively coupled Kelvin wave. This wave was instrumental in the abrupt termination of El Niño conditions in May 1998 and the establishment of convection at its more typical longitudes over the Maritime Continent (Takayabu et al. 1999; Kiladis and Straub 2003). As a result, rainfall over the SESA went from anomalously dry in May to wetter than normal in June. Because of the significant impact of the convectively coupled Kelvin wave on the 1998 SEAM, further work is underway to investigate the atmospheric budgets associated with this event. This analysis should help illuminate the heating and temperature relationships in this wave and provide a better understanding of its dynamics.

A regression analysis between the ENSO-3.4 SST index and monthly rainfall anomalies suggests that ENSO exerted a strong influence on the rainfall distribution during SCSMEX. Overall this resulted in wetter-than-

normal conditions along the south China coast and northern SCS, and generally drier-than-normal conditions elsewhere, particularly over the Philippine Islands.

To obtain surface fluxes, which serve as lower boundary conditions for the atmospheric budgets, JMA/GAME reanalysis estimates were adjusted toward flux measurements taken at two research vessels as described in JC02. Surface fluxes of sensible plus latent heat over the SESA averaged 112 W m^{-2} during the May–June 1998 period, which is comparable to that observed in the west Pacific during TOGA COARE. In contrast, over the NESAs, warm, moist air advecting over a cool ocean surface resulted in relatively weak fluxes (44 W m^{-2}) during this period.

Rainfall over the NESAs occurred primarily during two 10-day periods that were separated by about a weeklong break. These active periods over the NESAs were largely out of phase with rainfall over the SESA domain, which was characterized by a wet period associated with the passage of the convectively coupled Kelvin wave in mid-May, followed by a weeklong break and then several episodic rain events with increasingly higher rain rates. A high correlation (0.79) between the

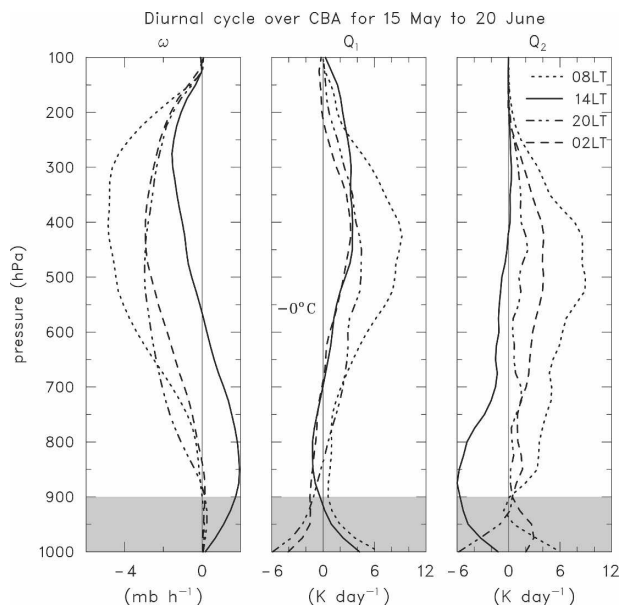


FIG. 19. Profiles of (left) vertical motion, (middle) Q_1 , and (right) Q_2 averaged over the CBA for the period 15 May–20 Jun 1998 as a function of the diurnal cycle: 0800 (dotted), 1400 (solid), 2000 (dashed–dotted), and 0200 LT (dashed). Results in shaded area below 900 hPa are less reliable; see text for details.

SESA-averaged TRMM and budget-derived rainfall time series indicates that the enhanced sounding network did a reasonable job of capturing the large-scale vertical motion field over the southern SCS. An even stronger correlation (0.95) between these rainfall estimates over the NESA is probably due to better TRMM and sounding coverage over this region.

Mean vertical motion, heating and moistening profiles averaged over the NESA were indicative of deep convection during the 15 May–20 June SCSMEX period. This observation, along with a surface-based radar analysis for the period 15–25 May, which found the stratiform fraction to be 26% (Johnson et al. 2005), suggests that the stratiform rain contribution over the NESA was considerably less than the 40% fraction typically observed in the Tropics (Schumacher and Houze 2003). Johnson et al. (2005) attribute this low stratiform fraction during the onset period to weak instability and relatively dry air in the upper troposphere, which would inhibit the development of large stratiform anvils. In turn, the dry air aloft over the northern SCS during this period was the result of dry, northwesterly flow on the east side of an upper-level anticyclone (Ding and Liu 2001).

In contrast, over the SESA, mean profiles of vertical motion showed weak low-level subsidence with an elevated peak in rising motion indicative of older precipitating cells. Moreover, the small vertical separation in

the Q_1 and Q_2 peaks along with the presence of low-level moistening and cooling indicates that SESA stratiform rain fraction during SCSMEX was likely quite significant and larger than that observed over the NESA. Cloud photographs and a weather log taken from a research vessel stationed in the southern SCS, along with large values of vertical eddy heat fluxes in the lower troposphere of the SESA, suggest that the ensemble of convection over this region consisted of alternating periods with decaying mesoscale systems with high stratiform fraction and shallow precipitating clouds. While sampling issues prohibit a meaningful analysis of TRMM PR data for the 47-day SCSMEX IOP, such an analysis for the May–June 1998–2003 period reveals about a 40% stratiform fraction in both the NESA and SESA regions (S. Nesbitt 2005, personal communication). Thus the low stratiform rain fraction over the NESA suggested by the results during SCSMEX may not be representative of the longer-term mean conditions.

Budget-derived values of tropospheric net-radiative heating for May–June 1998 indicate that the cooling rate over the NESA (-1.11 K day^{-1}) is more than double the SESA value (-0.47 K day^{-1}). The NESA value is suspiciously large and more typical of clear-sky conditions (Dopplack 1972). On the other hand, the SESA cooling rate compares favorably to budget-derived estimates from TOGA COARE (-0.55 K day^{-1}). While reasons for the significant disparity in cooling rates between these two regions are not certain, a few possible explanations include 1) the higher cirrus coverage over the SESA leading to smaller cooling rates through cloud longwave forcing, and 2) radiative effects due to smoke and haze from the immense Indonesian fires in the spring of 1998 (Simons 1998), which would also reduce longwave cooling to space.

The diurnal cycle of convection exhibits several prominent features over the SCS. Over the NESA, convection is initiated in the early morning hours along the south China coast. During the course of the day, convection gradually dissipates as it moves south and eastward over the NESA resulting in an early afternoon (1400 LT) rainfall peak. Over the southern SCS, the post-onset period was characterized by mesoscale convective systems developing off the west coast of Borneo in the early morning hours (0500–0800 LT). These systems propagate westward and dissipate over the course of the day resulting in a weak early afternoon (1400 LT) rainfall peak over the SESA. Further study of the diurnal cycle of convection over the SCS using several years of TRMM PR data, similar to that performed by Mori et al. (2004) over Sumatra, is warranted. Such an analysis would complement the budget analysis over

this region by revealing how the convective/stratiform rain fraction varies as the systems migrate away from the Borneo coast.

Finally, to facilitate the use of the budget-derived rainfall and latent heating products for TRMM validation purposes, and large-scale advective tendencies of temperature and moisture to force cloud-resolving models, these analyses have been made available at the following Web site: <http://tornado.atmos.colostate.edu/scsmex/>. An effort to improve these products for SCSMEX using constrained variational methods (Zhang and Lin 1997; Zhang et al. 2001) has been undertaken. This approach makes use of many supplementary data sources (e.g., rainfall estimates from multiple platforms such as ground-based radars, surface rain gauges, satellites, etc.) to constrain the budget analyses.

Acknowledgments. This research has been supported by the National Aeronautics and Space Administration under Grant NNG04GA22G and by the National Oceanic and Atmospheric Administration under Grant NA67RJ0152. We thank Dr. Wayne Schubert for his helpful discussions, Dr. Zhengzhao Luo for providing the cirrus data, Drs. Dave Parsons and James Pinto for providing the surface flux data from the research ships, Chelle Gentemann for providing the TMI SST data, and three anonymous reviewers for helpful comments on the manuscript.

REFERENCES

- Adler, R. F., and Coauthors, 2003: The version-2 Global Precipitation Climatology Project (GPCP) monthly precipitation analysis (1979–present). *J. Hydrometeorol.*, **4**, 1147–1167.
- Carbone, R. E., J. D. Tuttle, D. A. Ahijevych, and S. B. Trier, 2002: Inferences of predictability associated with warm season precipitation episodes. *J. Atmos. Sci.*, **59**, 2033–2056.
- Chan, J. C. L., Y. Wang, and J. Xu, 2000: Dynamic and thermodynamic characteristics associated with the onset of the 1998 South China Sea summer monsoon. *J. Meteor. Soc. Japan*, **78**, 367–380.
- , W. Ai, and J. Xu, 2002: Mechanisms responsible for the maintenance of the 1998 South China Sea summer monsoon. *J. Meteor. Soc. Japan*, **80**, 1103–1113.
- Chang, C.-P., and G. T.-J. Chen, 1995: Tropical circulations associated with southwest monsoon onset and westerly surges over the South China Sea. *Mon. Wea. Rev.*, **123**, 3254–3267.
- Chen, T.-C., and M. Murakami, 1988: The 30–50 day variation of convective activity over the western Pacific Ocean with emphasis on the northwestern region. *Mon. Wea. Rev.*, **116**, 892–906.
- , and J.-M. Chen, 1995: An observational study of the South China Sea monsoon during the 1979 summer. *Mon. Wea. Rev.*, **123**, 2295–2318.
- , and S.-P. Weng, 1999: Interannual and intraseasonal variations in monsoon depressions and their westward-propagating predecessors. *Mon. Wea. Rev.*, **127**, 1005–1020.
- , M.-C. Yen, and S.-P. Weng, 2000: Interaction between the summer monsoons in east Asia and the South China Sea: Intraseasonal monsoon modes. *J. Atmos. Sci.*, **57**, 1373–1392.
- Ciesielski, P. E., R. H. Johnson, P. T. Haertel, and J. Wang, 2003: Corrected TOGA COARE sounding humidity data: Impact on diagnosed properties of convection and climate over the warm pool. *J. Climate*, **16**, 2370–2384.
- Ding, Y.-H., and J. Hu, 1988: The variation of the heat sources in east Asia in the early summer of 1984 and their effects on the large-scale circulation in east Asia. *Adv. Atmos. Sci.*, **6**, 171–180.
- , and X.-F. Wang, 1988: An analysis of the distribution of apparent heat sources and sinks over the middle reaches of Yangtze River during the Meiyu season in 1983 (in Chinese). *Trop. Meteor.*, **4**, 134–145.
- , and Y. Liu, 2001: Onset and evolution of the summer monsoon over the South China Sea during SCSMEX field experiment in 1998. *J. Meteor. Soc. Japan*, **79**, 255–276.
- Dopplick, T. G., 1972: Radiative heating of the global atmosphere. *J. Atmos. Sci.*, **29**, 1278–1294.
- Fein, J. S., and J. P. Kuettner, 1980: Report on the summer MONEX field phase. *Bull. Amer. Meteor. Soc.*, **61**, 461–474.
- Fukutomi, Y., and T. Yasunari, 1999: 10–25 day intraseasonal variations of convection and circulation over east Asia and western North Pacific during early summer. *J. Meteor. Soc. Japan*, **77**, 753–769.
- Houze, R. A., Jr., S. G. Geotis, F. D. Marks Jr., and A. K. West, 1981: Winter monsoon convection in the vicinity of North Borneo. Part 1: Structure and time variation of the clouds and precipitation. *Mon. Wea. Rev.*, **109**, 1595–1614.
- Huffman, G. J., and Coauthors, 2001: Global precipitation at one-degree daily resolution from multisatellite observations. *J. Hydrometeorol.*, **2**, 36–50.
- , R. F. Adler, S. Curtis, D. T. Bolvin, and E. J. Nelkin, 2005: Global rainfall analyses at monthly and 3-hr time scales. *Measuring Precipitation from Space: EURAINSAT and the Future*, V. Levizzani, P. Bauer, and J. Turk, Eds., Kluwer Academic, in press.
- Ichikawa, H., and T. Yasunari, 2004: Time–space characteristics of diurnal rainfall activity over Indonesian maritime continent. *Proc. Second TRMM Int. Science Conf.*, Nara, Japan, Japan Aerospace Exploration Agency, CD-ROM, 4.4.
- Johnson, R. H., 1980: Diagnosis of convective and mesoscale motions during phase III of GATE. *J. Atmos. Sci.*, **37**, 733–753.
- , and G. S. Young, 1983: Heat and moisture budgets of tropical mesoscale anvil clouds. *J. Atmos. Sci.*, **40**, 2138–2147.
- , and P. E. Ciesielski, 2000: Rainfall and radiative heating rate estimates from TOGA COARE atmospheric budgets. *J. Atmos. Sci.*, **57**, 1497–1514.
- , and —, 2002: Characteristics of the 1998 summer monsoon onset over the northern South China Sea. *J. Meteor. Soc. Japan*, **80**, 561–578.
- , Z. Wang, and J. F. Bresch, 1993: Heat and moisture budgets over China during the early summer monsoon. *J. Meteor. Soc. Japan*, **71**, 137–152.
- , S. L. Aves, S. L. Nesbitt, and P. E. Ciesielski, 2004: The diurnal cycle of precipitation over the northern South China Sea. *Proc. Second TRMM Int. Science Conf.*, Nara, Japan, Japan Aerospace Exploration Agency, CD-ROM, 4.3.
- , —, P. E. Ciesielski, and T. D. Keenan, 2005: Organization of oceanic convection during the onset of the 1998 east Asian summer monsoon. *Mon. Wea. Rev.*, **133**, 131–148.
- Kato, K., 1985: On the abrupt change in the structure of the Baiu

- front over the China continent in late May of 1979. *J. Meteor. Soc. Japan*, **63**, 20–36.
- Kiladis, G. N., and K. H. Straub, 2003: Ocean–atmosphere interaction within equatorially trapped atmospheric waves. Preprints, *12th Conf. on the Interaction of the Sea and Atmosphere*, Long Beach, CA, Amer. Meteor. Soc., CD-ROM, J1.7.
- Kummerow, C., and Coauthors, 2000: The status of the Tropical Rainfall Measuring Mission (TRMM) after two years in orbit. *J. Appl. Meteor.*, **39**, 1965–1982.
- Lau, K.-M., and P. H. Chan, 1986: Aspects of the 40–50 day oscillation during the northern summer as inferred from outgoing longwave radiation. *Mon. Wea. Rev.*, **114**, 1354–1367.
- , and S. Yang, 1997: Climatology and interannual variability of the Southeast Asian Summer Monsoon. *Adv. Atmos. Sci.*, **14**, 141–162.
- , and H. T. Wu, 2001: Principal modes of rainfall–SST variability of the Asian summer monsoon: A reassessment of the monsoon–ENSO relationship. *J. Climate*, **14**, 2880–2895.
- , G. J. Yang, and S. H. Shen, 1988: Seasonal and intraseasonal climatology of summer monsoon rainfall over east Asia. *Mon. Wea. Rev.*, **116**, 18–37.
- , and Coauthors, 2000: A report of the field operations and early results of the South China Sea Monsoon Experiment (SCSMEX). *Bull. Amer. Meteor. Soc.*, **81**, 1261–1270.
- Lawrence, D. M., and P. J. Webster, 2002: The boreal summer intraseasonal oscillation: Relationship between northward and eastward movement of convection. *J. Atmos. Sci.*, **59**, 1593–1606.
- Li, C., and J. Wu, 2000: On the onset of the South China Sea summer monsoon in 1998. *Adv. Atmos. Sci.*, **17**, 193–204.
- Liebmann, B., and C. A. Smith, 1996: Description of a complete (interpolated) outgoing longwave radiation dataset. *Bull. Amer. Meteor. Soc.*, **77**, 1275–1277.
- Loechl, E. R., 2000: Equatorial and subtropical waves and the onset of the southeast Asian monsoon. Preprints, *24th Conf. on Hurricanes and Tropical Meteorology*, Fort Lauderdale, FL, Amer. Meteor. Soc., 583–584.
- Luo, H.-B., and M. Yanai, 1983: The large-scale circulation and heat sources over the Tibetan Plateau and surrounding areas during the early summer of 1979. Part I: Precipitation and kinematic analyses. *Mon. Wea. Rev.*, **111**, 922–944.
- , and —, 1984: The large-scale circulation and heat sources over the Tibetan Plateau and surrounding areas during the early summer of 1979. Part II: Heat and moisture budgets. *Mon. Wea. Rev.*, **112**, 966–989.
- Luo, Z., and W. B. Rossow, 2004: Characterizing tropical cirrus lifecycles, evolution and interaction with upper tropospheric water vapor using Lagrangian trajectory analysis of satellite observations. *J. Climate*, **17**, 4541–4563.
- Mapes, B. E., 2000: Convective inhibition, subgrid-scale triggering energy, and stratiform instability in a toy tropical wave model. *J. Atmos. Sci.*, **57**, 1515–1535.
- , and R. A. Houze Jr., 1995: Diabatic divergence profiles in western Pacific mesoscale convective systems. *J. Atmos. Sci.*, **52**, 1807–1828.
- , T. T. Warner, and M. Xu, 2003: Diurnal patterns of rainfall in northwestern South America. Part III: Diurnal gravity waves and nocturnal convection offshore. *Mon. Wea. Rev.*, **131**, 830–844.
- Mori, S., and Coauthors, 2004: Diurnal land–sea rainfall peak migration over Sumatera Island, Indonesian Maritime Continent, observed by TRMM satellite and intensive rawinsonde soundings. *Mon. Wea. Rev.*, **132**, 2021–2039.
- Nieto Ferreira, R., W. H. Schubert, and J. J. Hack, 1996: Dynamical aspects of twin tropical cyclones associated with the Madden–Julian oscillation. *J. Atmos. Sci.*, **53**, 929–945.
- Nitta, T., 1987: Convective activities in the tropical western Pacific and their impact on the Northern Hemisphere summer circulation. *J. Meteor. Soc. Japan*, **65**, 373–390.
- Olson, W. O., C. D. Kummerow, Y. Hong, and W.-K. Tao, 1999: Atmospheric latent heating distributions in the Tropics derived from satellite passive microwave radiometer measurements. *J. Appl. Meteor.*, **38**, 633–664.
- Randall, D. A., Harshvardhan, D. A. Dazlich, and T. G. Corsetti, 1989: Interactions among radiation, convection and large-scale dynamics in a general circulation model. *J. Atmos. Sci.*, **46**, 1943–1970.
- , —, and —, 1991: Diurnal variability of the hydrologic cycle in a general circulation model. *J. Atmos. Sci.*, **48**, 41–62.
- Raymond, D. J., 2000: The Hadley circulation as a radiative–convective instability. *J. Atmos. Sci.*, **57**, 1286–1297.
- Schumacher, C., and R. A. Houze Jr., 2003: Stratiform rain in the Tropics as seen by the TRMM Precipitation Radar. *J. Climate*, **16**, 1739–1756.
- Shige, S., Y. N. Takayabu, W.-K. Tao, and D. E. Johnson, 2004: Spectral retrieval of latent heating profiles from TRMM PR data. Part I: Development of a model-based algorithm. *J. Appl. Meteor.*, **43**, 1095–1113.
- Simons, L. M., 1998: Indonesia’s plague of fire. *National Geographic*, No. 194, 100–119.
- Straub, K. H., and G. N. Kiladis, 2003: The observed structure of convectively coupled Kelvin waves: Comparison with simple models of coupled wave instability. *J. Atmos. Sci.*, **60**, 1655–1668.
- Takayabu, Y. N., T. Iguchi, M. Kachi, A. Shibata, and H. Kanazawa, 1999: Abrupt termination of the 1997–98 El Niño in response to a Madden–Julian oscillation. *Nature*, **402**, 279–282.
- Tao, S. Y., and L. X. Chen, 1987: A review of recent research on the east Asian summer monsoon in China. *Monsoon Meteorology III*, C.-P. Chang, and T. N. Krishnamurti, Eds., Oxford University Press, 60–92.
- Tao, W.-K., C.-L. Shie, J. Simpson, S. Braun, R. H. Johnson, and P. E. Ciesielski, 2003: Convective systems over the South China Sea: Cloud-resolving model simulations. *J. Atmos. Sci.*, **60**, 2929–2956.
- Thompson, R. M., Jr., S. W. Payne, E. E. Recker, and R. J. Reed, 1979: Structure and properties of synoptic-scale wave disturbances in the intertropical convergence zone of the eastern Atlantic. *J. Atmos. Sci.*, **36**, 53–72.
- Wang, B., L. Ho, Y. Zhang, and M.-M. Lu, 2004: Definition of the South China Sea monsoon onset and commencement of the east Asia summer monsoon. *J. Climate*, **17**, 699–710.
- Wang, J.-J., 2004: Evolution and structure of the mesoscale convection and its environment: A case study during the early onset of the southeast Asian summer monsoon. *Mon. Wea. Rev.*, **132**, 1104–1120.
- Wentz, F. J., C. Gentemann, D. Smith, and D. Chelton, 2000: Satellite measurements of sea surface temperature through clouds. *Science*, **288**, 847–850.
- Wu, G., and Y. Zhang, 1998: Tibetan plateau forcing and the timing of the monsoon onset over south Asia and the South China Sea. *Mon. Wea. Rev.*, **126**, 913–927.

- Yamazaki, N., and Coauthors, 2000: On the release of GAME Reanalysis products (in Japanese). *Tenki*, **47**, 659–663.
- Yanai, M., and Y. Hayashi, 1969: Large-scale equatorial waves penetrating from the upper troposphere into the lower stratosphere. *J. Meteor. Soc. Japan*, **47**, 167–182.
- , and R. H. Johnson, 1993: Impacts of cumulus convection on thermodynamic fields. *The Representation of Cumulus Convection in Numerical Models of the Atmosphere, Meteor. Monogr.*, No. 46, Amer. Meteor. Soc., 39–62.
- , and T. Tomita, 1998: Seasonal and interannual variability of atmospheric heat sources and moisture sinks determined from NCEP–NCAR reanalysis. *J. Climate*, **11**, 463–482.
- , S. Esbensen, and J. H. Chu, 1973: Determination of bulk properties of tropical cloud clusters from large-scale heat and moisture budgets. *J. Atmos. Sci.*, **30**, 611–627.
- , C. Li, and Z. Song, 1992: Seasonal heating of the Tibetan Plateau and its effects on the evolution of the Asian summer monsoon. *J. Meteor. Soc. Japan*, **70**, 319–351.
- Zhang, M. H., and J. L. Lin, 1997: Constrained variational analysis of sounding data based on column-integrated conservations of mass, heat, moisture, and momentum: Approach and application to ARM measurements. *J. Atmos. Sci.*, **54**, 1503–1524.
- , —, R. T. Cederwall, J. J. Yio, and S. C. Xie, 2001: Objective analysis of ARM IOP data: Method and sensitivity. *Mon. Wea. Rev.*, **129**, 295–311.